Nano Research

Open Access

Research Article

Molecular interlayer engineering of VSe_2 enables fast and durable magnesium–lithium hybrid ion storage

Jiu-Long Li[1,2,§], Li-Rong Wang[1,2,§], You-Quan Jiang[1,2], Chao-Yu Chen[1,2], Hao-Nan Song[1,2], Yan-Jun Xing[1,2], Zhao-Dong Li[1,2,3,4] ✉, and Sheng Liu[1,2,3,4] ✉

[1] *School of Integrated Circuits, Wuhan University, Wuhan 430072, China*
[2] *The Institute of Technological Sciences, Wuhan University, Wuhan 430072, China*
[3] *School of Power and Mechanical Engineering, Wuhan University, Wuhan 430072, China*
[4] *Hubei Key Laboratory of Electronic Manufacturing and Packaging Integration, Wuhan University, Wuhan 430072, China*
[§] *Jiu-Long Li and Li-Rong Wang contributed equally to this work.*

Cite this article: *Nano Research*, **2026**, *19*, 94908829. https://doi.org/10.26599/NR.2026.94908829

ABSTRACT: Vanadium diselenide (VSe_2) is a promising cathode material for magnesium–lithium hybrid batteries (MLHB), owing to its favorable electronic structure and layered framework. However, practical Mg^{2+} storage is hindered by narrow interlayer spacing, strong Mg^{2+} host Coulombic interactions, and structural degradation during repeated ion insertion. Here, we introduce a molecular interlayer engineering strategy based on ethylenediamine (EDA) intercalation to address these challenges. A combination of theoretical calculations and experimental investigations reveals that EDA modification simultaneously expands the interlayer spacing, modulates the electronic structure, and weakens the Coulombic interactions between the lattice and the guest ions, thereby facilitating Mg^{2+}/Li^+ diffusion and enhancing reaction kinetics. Moreover, the electron-rich $–NH_2$ groups of EDA engage in reversible chelation with the guest ions, providing additional storage sites and enabling an inorganic–organic synergistic storage mechanism based on topological intercalation reactions. As a result, the optimized EDA-intercalated VSe_2 (E(0.2)-VSe_2) cathode exhibits a stable capacity of 82.5 mAh·g^{-1} over 4500 cycles at 1000 mA·g^{-1}, with a remarkable capacity retention of 72.7%. This work underscores molecular interlayer engineering as an effective strategy for enhancing the performance of layered cathodes in multivalent rechargeable batteries.

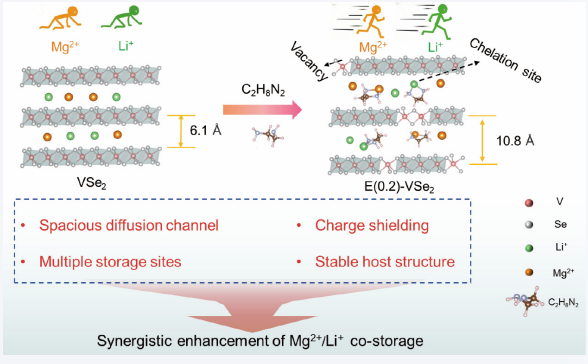

KEYWORDS: magnesium–lithium hybrid batteries, transition metal chalcogenides, interlayer modification, dual-ion storage

1 Introduction

Magnesium-based batteries are widely regarded as a compelling alternative to lithium-ion technology for large-scale energy storage, owing to the high volumetric capacity, natural abundance, and intrinsic safety of Mg metal anodes [1–3]. Despite decades of intensive research, however, the realization of practical rechargeable magnesium batteries (RMB) remains elusive. The fundamental obstacle arises from the divalent nature of Mg^{2+}: Its strong electrostatic interaction with host lattices results in sluggish solid-state diffusion, high desolvation barriers, and pronounced lattice polarization, collectively undermining rate capability and reversibility in intercalation-type cathodes [4–7].

Hybridizing Mg^{2+} with monovalent ions offers a promising pathway to partially alleviate these constraints. Magnesium–lithium hybrid batteries (MLHB) exploit the rapid intercalation kinetics of Li^+ to activate host structures while retaining the high capacity and safety advantages of magnesium metal anodes [8, 9]. Nevertheless, even in hybrid systems, cathode performance remains fundamentally limited by the inefficient accommodation of Mg^{2+} with high charge density. This challenge underscores a central design question: How can cathode materials be engineered to effectively screen Mg^{2+} electrostatics without compromising structural integrity or energy density?

Layered transition-metal dichalcogenides (TMDC) provide an

Received: March 7, 2026; **Revised:** April 21, 2026
Accepted: May 12, 2026

✉Address correspondence to Sheng Liu, shengliu@whu.edu.cn; Zhao-Dong Li, Zhaodong_Li@whu.edu.cn

attractive platform to address this challenge due to their tunable van der Waals gaps, adjustable bandgaps, and phase tunability [10–13]. Among them, vanadium diselenide (VSe_2) is particularly promising owing to its metallic 1T phase, high electronic conductivity [14], relatively open interlayer spacing, and the lower electronegativity of selenium compared with sulfur and oxygen [15–17]. Yet, these intrinsic advantages remain insufficient to overcome the strong Mg^{2+}–host interactions. Even with Li^+ co-intercalation, Mg^{2+} insertion into VSe_2 is kinetically hindered and structurally disruptive, leading to limited rate performance and rapid capacity decay [18].

Conventional strategies to improve Mg^{2+} storage, including morphology control [19–22], defect engineering [23–25], elemental doping [26, 27], and surface modification [28], primarily target transport length scales, interfacial reactivity, or volume change mitigation. However, these approaches do not fundamentally address the strong Coulombic interactions between Mg^{2+} and the VSe_2 framework. Moreover, the limited interlayer spacing of VSe_2 makes it difficult for these modification strategies to push the capacity beyond the theoretical limit of the material. Interlayer engineering offers a more direct strategy for improving guest-ion storage and transport by expanding the available storage space. The enlarged interlayer space not only weakens the electrostatic interaction between guest ions and the host framework but also accommodates more guest ions, which may enable additional ion storage beyond the theoretical capacity limit. However, existing approaches introduce new trade-offs. Pre-intercalated ions or solvent molecules often suffer from electrochemical instability [29–31], while inert organic or inorganic spacers occupy active sites, impose steric hindrance, and suppress effective ion intercalation [32–36], ultimately limiting energy density and cycling stability [37]. These limitations highlight the need for interlayer modifiers that simultaneously provide structural stabilization, electrostatic screening, and electrochemical activity.

Here, we report a molecular interlayer engineering strategy for VSe_2 based on ethylenediamine (EDA) intercalation that addresses these requirements (Fig. 1). As a lightweight bidentate ligand with electron-rich amine groups, EDA expands the interlayer spacing, modulates the local electronic environment, and effectively screens the high charge density of Mg^{2+}. Concurrently, EDA functions as a molecular pillar that stabilizes the layered framework during repeated guest-ion insertion and extraction. Furthermore, it offers additional storage sites through reversible chelation/dissociation with guest ions, thereby establishing a synergistic inorganic–organic charge storage mechanism. By synergistically regulating dual-ion transport kinetics through electrostatic screening, structural stabilization, and multisite storage within a unified interlayer architecture, this strategy markedly enhances both the rate capability and long-term cycling stability of VSe_2 cathodes in MLHB.

2 Results and discussion

Density functional theory (DFT) calculations were performed to provide mechanistic insight into the role of EDA as an intercalated guest within the VSe_2 interlayer. As shown in Fig. 2(a), the electrostatic potential (ESP) distribution of the EDA molecule reveals that the two primary $–NH_2$ groups are rich in lone-pair electrons and exhibit regions of highly negative electrostatic potential, confirming their strong electron-donating capability. These electron-rich sites display a strong affinity for cations (Mg^{2+} and Li^+), endowing EDA-intercalated VSe_2 (E-VSe_2) with an enhanced ability to coordinate guest ions and indicating the emergence of a synergistic inorganic–organic charge-storage mechanism. To quantify the thermodynamic stability of ion insertion, formation energies were calculated for Mg^{2+} intercalation, Li^+ intercalation, and Mg^{2+}/Li^+ co-intercalation in both pristine VSe_2 and E-VSe_2 (Fig. 2(b)). Structurally, both Mg^{2+} and Li^+ tend to bind to EDA molecules in chelating configurations within the E-VSe_2 interlayer. For the Mg^{2+}/Li^+ co-intercalation system, the results reveal that configurations in which Mg^{2+} and Li^+ are coordinated by separate EDA molecules are energetically more favorable than configurations in which they share a single EDA molecule (Fig. S1

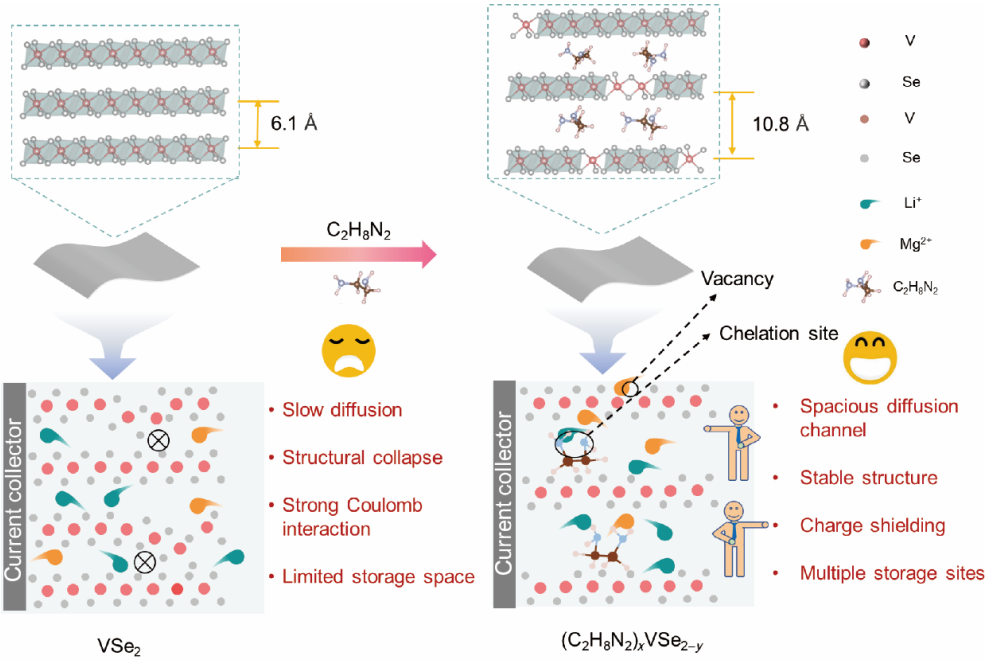

Figure 1 Schematic diagram of the EDA interlayer modification strategy for VSe_2 to improve the Mg^{2+}/Li^+ storage environment and enhance storage kinetics in MLHB.

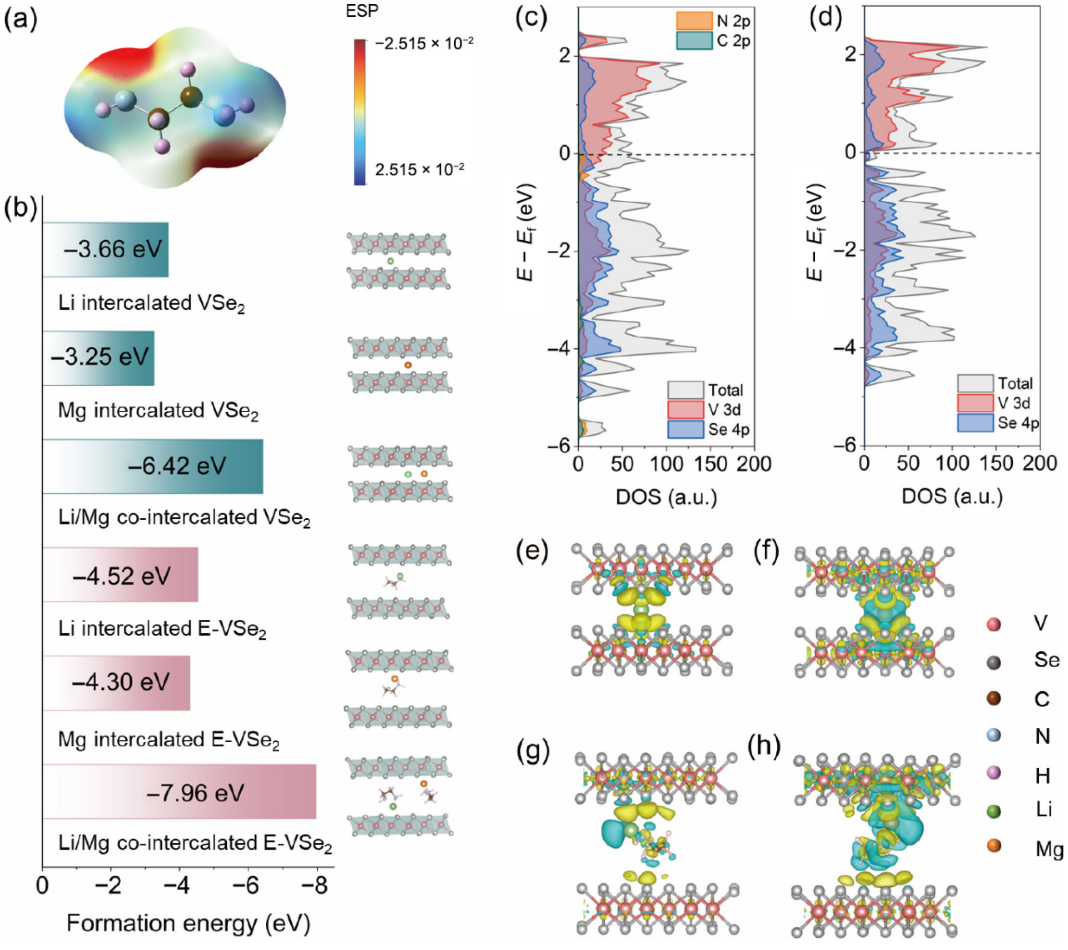

Figure 2 (a) ESP of the EDA molecule. (b) Formation energy diagram of Mg^{2+}/Li^{+} intercalated E-VSe_2 and atomic configurations. DOS of (c) E-VSe_2 and (d) VSe_2. Charge density difference diagrams for (e) Li^{+} and (f) Mg^{2+} intercalated VSe_2, and for (g) Li^{+} and (h) Mg^{2+} intercalated E-VSe_2 (isosurface: 0.001).

in the Electronic Supplementary Material (ESM)). Specifically, the calculated formation energies for Li^{+} intercalation, Mg^{2+} intercalation, and Mg^{2+}/Li^{+} co-intercalation in E-VSe_2 are −4.52, −4.30, and −7.96 eV, respectively, markedly lower than the corresponding values in pristine VSe_2 (−3.66, −3.25, and −6.42 eV). This pronounced energetic stabilization demonstrates that guest-ion intercalation is thermodynamically more favorable in the EDA-modified interlayer environment, yielding a more stable host structure. The resulting framework provides robust and continuous ion-transport channels, ensuring sustained capacity output and facilitating subsequent multivalent-ion intercalation.

To elucidate the impact of interlayer modification on the electronic structure of VSe_2, density of states (DOS) calculations were performed for both E-VSe_2 and pristine VSe_2, as shown in Figs. 2(c) and 2(d). In both systems, the non-zero DOS at the Fermi level confirms their metallic properties and high electronic conductivity. Compared with pristine VSe_2, E-VSe_2 displays a markedly increased DOS near the Fermi level, indicating an increased density of accessible electronic states. Partial DOS (PDOS) analysis further reveals that N 2p orbitals from EDA contribute directly near the Fermi level, indicating strong electronic coupling between the organic intercalant and the V–Se framework. Charge density difference analysis (Fig. S2 in the ESM) provides direct visualization of electron transfer from EDA molecules to the V–Se layers, signifying pronounced interfacial charge coupling within E-VSe_2. Such charge redistribution is expected to promote charge transport. Here, yellow and cyan regions correspond to charge accumulation and charge depletion, respectively. The presence of EDA also markedly alters the electrostatic interaction between intercalated ions and the host lattice, as revealed by charge density difference maps for Mg^{2+} and Li^{+} intercalation (Figs. 2(e)–2(h)). In pristine VSe_2, pronounced charge accumulation and depletion are localized around the intercalated Mg^{2+} and Li^{+} and their neighboring Se and V atoms, with this effect being especially severe for Mg^{2+}, indicative of strong electrostatic interaction with the VSe_2 layers. By contrast, the intercalated EDA molecules in E-VSe_2 effectively screen the Mg^{2+} and Li^{+} from direct Coulombic interaction with the V–Se framework. Charge redistribution is instead concentrated at the interface between the EDA molecules and the V–Se layers on the ion-facing side, forming an electrostatic buffer layer surrounding the guest ions. This shielding effect substantially weakens ion-host electrostatic interactions, thereby creating favorable kinetic conditions for rapid guest-ion diffusion within the expanded interlayer space. Additionally, Fig. S3 in the ESM further shows electron depletion within the EDA molecules and electron accumulation at the Mg^{2+} and Li^{+}, confirming the strong electron-donating nature of EDA and its critical role in electrostatic screening and ion storage.

E(0.2)-VSe_2 was synthesized via a facile two-step strategy (Fig. S4 in the ESM). In the first step, VSe_2 nanosheets were obtained through a wet-chemical route in oleylamine, yielding well-defined two-dimensional morphologies (Fig. 3(a)). Subsequently, EDA

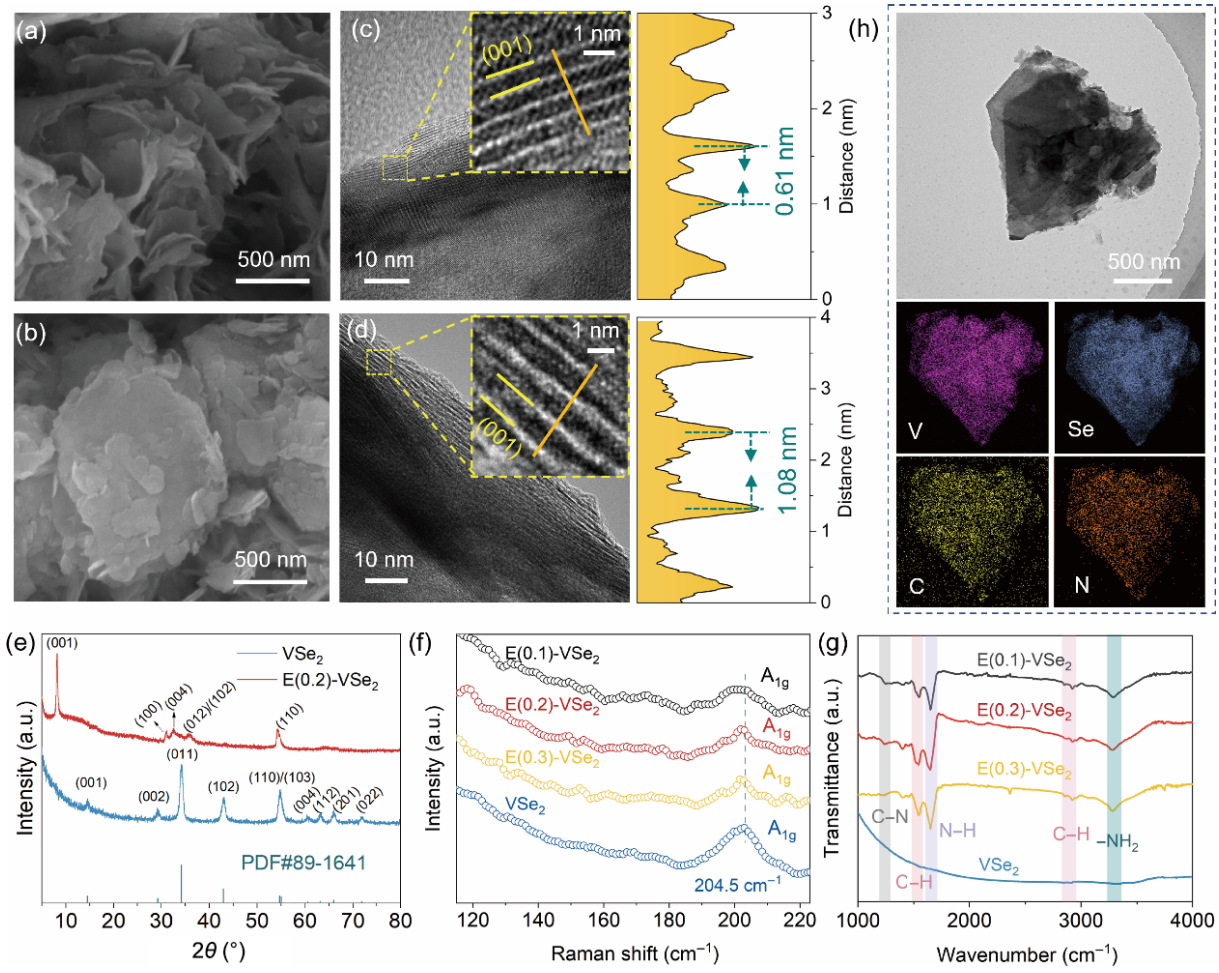

Figure 3 Scanning electron microscopy (SEM) images of (a) VSe_2 and (b) E(0.2)-VSe_2. HRTEM images of (c) VSe_2 and (d) E(0.2)-VSe_2 with corresponding magnified views. (e) XRD patterns, (f) Raman spectra, and (g) FTIR spectra of VSe_2 and E(0.2)-VSe_2. (h) TEM morphology of an E(0.2)-VSe_2 nanosheet and its corresponding TEM-EDS elemental mapping.

molecules were intercalated into the interlayer galleries of VSe_2 through a high-temperature, high-pressure infiltration process. The resulting E(0.2)-VSe_2 preserves the nanosheet morphology of pristine VSe_2 (Fig. 3(b)), accompanied by a slight increase in thickness, which is attributed to interlayer expansion and partial restacking induced during EDA intercalation. High-resolution transmission electron microscopy (HRTEM) reveals well-resolved (001) lattice fringes, and the corresponding intensity profiles (Figs. 3(c) and 3(d)) demonstrate a pronounced interlayer expansion of 180.3% in E(0.2)-VSe_2 relative to pristine VSe_2, with the *d*-spacing increased to 1.08 nm. This structural expansion is further supported by the X-ray diffraction (XRD) patterns (Fig. 3(e)). The Miller indices of the diffraction peaks of E(0.2)-VSe_2 are confirmed by Le Bail refinement (Fig. S5 and Table S1 in the ESM), in which the (001) reflection of E(0.2)-VSe_2 shifts to a lower diffraction angle of 8.2°. Notably, the interlayer spacing of E-VSe_2 can be precisely tuned by varying the EDA/VSe_2 feeding ratio, with linear expansion observed as the ratio increases (Fig. S6 in the ESM). Specifically, the interlayer spacings of E(0.1)-VSe_2 and E(0.3)-VSe_2 are 1.13 and 0.98 nm, respectively, demonstrating the high controllability of the interlayer engineering process. Raman spectroscopy shows that the A_{1g} out-of-plane stretching mode of pristine VSe_2 appears at 204.5 cm^{-1} (Fig. 3(f)). Upon EDA intercalation, this mode exhibits a pronounced red shift in E-VSe_2 (Table S2 in the ESM), indicative of reduced vibrational energy, enhanced local disorder, and weakened interlayer van der Waals interactions [38, 39]. Such changes provide a favorable structural basis for lowering the energy barrier of guest-ion intercalation, underscoring the effectiveness of EDA-mediated interlayer modification. Fourier-transform infrared (FTIR) spectroscopy (Fig. 3(g)) further verifies the successful incorporation of EDA within the expanded interlayers, as evidenced by characteristic transmittance peaks corresponding to C–N stretching vibration (1253.5 cm^{-1}), C–H stretching vibrations (1550.5, 2850.4, and 2919.8 cm^{-1}), N–H bending vibration (1650.8 cm^{-1}), and $-NH_2$ stretching vibration (3290.1 cm^{-1}) [39, 40]. Energy-dispersive X-ray spectroscopy (EDS) elemental mapping (Fig. 3(h)) confirms the homogeneous distribution of V, Se, N, and C throughout the E(0.2)-VSe_2 nanosheets. In contrast, no N signal is detected in pristine VSe_2; only V, Se, and C signals are observed (Fig. S7 in the ESM). The C map is markedly distorted compared with the V and Se maps, which indicates that this C signal mainly originates from the carbon film on the copper grid and may also partly arise from residual solvent from the synthesis process remaining on the sample surface. Quantitative elemental analysis (EA) reveals an EDA content of approximately 11 wt.% based on a measured N content of 5.17 wt.%, in good agreement with thermogravimetric analysis (TGA) results (Fig. S8 in the ESM). These measurements

collectively confirm the chemical formula of the intercalation compound as $(C_2H_8N_2)_{0.43}VSe_2$.

The valence states of V and Se were further investigated by X-ray photoelectron spectroscopy (XPS). As shown in Fig. S9 in the ESM, E(0.2)-VSe_2 exhibits an increased proportion of V^{2+} species, which correlates closely with the formation of selenium vacancies. These vacancies are attributed to the reducing ability of EDA, which disrupts some V–Se bonds during thermal treatment, leading to the removal of Se atoms from the lattice. This interpretation is further supported by electron paramagnetic resonance (EPR) spectroscopy (Fig. S10 in the ESM), which reveals a higher concentration of paramagnetic defects in E(0.2)-VSe_2 relative to pristine VSe_2. The introduction of Se vacancies is expected to increase the density of electrochemically active sites and enhance the adsorption affinity toward guest ions within the VSe_2 framework. Such defect-mediated activation has been widely recognized as beneficial for multivalent-ion storage [17, 41, 42]. To evaluate the specific surface area and pore size distribution of the materials, N_2 adsorption–desorption measurements were performed (Fig. S11 in the ESM). The specific surface area of E(0.2)-VSe_2 is smaller than that of pristine VSe_2, which is most likely due to the partial restacking of nanosheets during the post-synthesis treatment. Meanwhile, the pore volume in the 2–15 nm range increases significantly. This increased pore volume is closely associated with the formation of Se vacancies. However, the lower specific surface area reduces the effective contact area between the electrode material and the electrolyte, while also limiting the number of exposed active sites in the initial state. This may suppress rapid ion adsorption and interfacial charge transfer, while limiting bulk-phase reactions, and thereby constraining the initial capacity of the electrode. Therefore, the electrode may need to undergo a pronounced activation process before its intrinsic capacity and reaction kinetics can be fully manifested [43, 44]. Based on the above characteristics, the results indicate that the meticulously engineered E(0.2)-VSe_2, which integrates interlayer expansion and defect modulation, provides a highly advantageous host environment for storing complex mixed guest ions.

Based on the predicted advantages of EDA-modified interlayers in VSe_2, as indicated by DFT calculations, MLHB were assembled using materials with varying EDA contents. The electrochemical performance of these EDA-modified VSe_2 cathodes was systematically evaluated. As shown in Fig. 4(a), cycling performance over 200 cycles was assessed at a low current density of 200 mA·g^{-1}. Although the pristine VSe_2 cathode exhibits a high initial capacity, its capacity decays rapidly within the first 20 cycles, ultimately reaching a low residual capacity of only 66.6 mAh·g^{-1} after 200 cycles. This rapid degradation is attributed to the deterioration of the interlayer structure and the retention of guest ions. By contrast, the E-VSe_2 cathodes demonstrate improved cycling stability and higher specific capacity (Fig. S12 in the ESM). Notably,

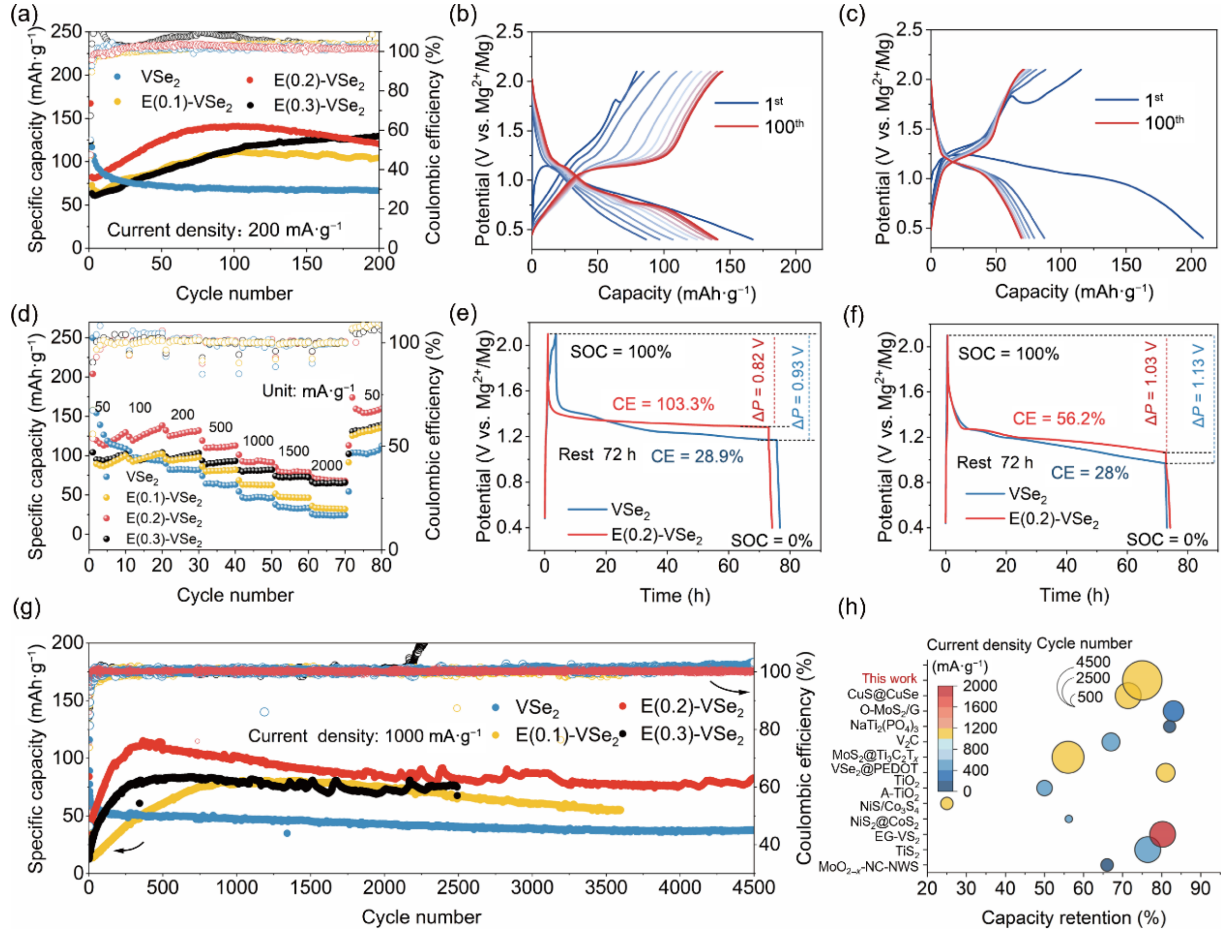

Figure 4 (a) The short cycle performance of VSe_2, E(0.1)-VSe_2, E(0.2)-VSe_2, and E(0.3)-VSe_2 at 200 mA·g^{-1}. The charge–discharge curves for (b) E(0.2)-VSe_2 and (c) pristine VSe_2 from the 1st to 100th cycle, sampled every 10 cycles. (d) The rate capability of VSe_2, E(0.1)-VSe_2, E(0.2)-VSe_2, and E(0.3)-VSe_2 at varying current densities. ((e) and (f)) The self-discharge curves at the 1st and 100th cycles for E(0.2)-VSe_2 and pristine VSe_2. (g) The long-cycle performance of VSe_2, E(0.1)-VSe_2, E(0.2)-VSe_2, and E(0.3)-VSe_2 at 1000 mA·g^{-1}. (h) Comparison of electrochemical performance between E(0.2)-VSe_2 and previously reported MLHB cathodes.

the E(0.2)-VSe_2 cathode outperforms both the E(0.1)-VSe_2 and E(0.3)-VSe_2 electrodes. It achieved a maximum specific capacity of 141.2 mAh·g^{-1} and retained 120.2 mAh·g^{-1} after 200 cycles, representing an 80.5% improvement compared with the pristine VSe_2 cathode. For E(0.2)-VSe_2 (Fig. 4(b)), the sloping charge–discharge curves without obvious voltage plateaus in the early stage of cycling preliminarily indicate that the charge-storage process is dominated by pseudocapacitive behavior arising from fast surface or near-surface reactions [45], in stark contrast to the distinct discharge plateau observed in the initial cycle of pristine VSe_2 (Fig. 4(c)). However, as cycling proceeds, the charge–discharge plateaus of E(0.2)-VSe_2 become more defined, indicating a typical activation process. This may be attributed to the smaller specific surface area of materials, which limits the initial electrode–electrolyte contact area and the number of accessible active sites. In addition, EDA molecules may initially occupy the entrances of the interlayer channels. These factors can delay complete electrolyte wetting and full electrochemical activation of the host. As a result, bulk reactions are restricted, and energy storage is dominated by surface reactions during the early stage. Therefore, the electrode capacity cannot be fully delivered during the initial cycles before the activation process is completed. As cycling proceeds, the electrode/electrolyte interface gradually stabilizes, wettability improves, interlayer transport pathways become more accessible, and additional active sites are exposed, which increases the contribution of bulk reactions and leads to a gradual increase in capacity [43, 44, 46]. In addition, the sudden drop in voltage during the first discharge and its subsequent recovery are mainly attributed to voltage hysteresis caused by the passivation of the Mg anode [47, 48].

Upon increasing the current density to 500 mA·g^{-1}, the E(0.2)-VSe_2 electrode maintains a stable capacity of 129.8 mAh·g^{-1} over 600 cycles. By comparison, pristine VSe_2 retains only 49.1% of this capacity under identical conditions (Fig. S13 in the ESM), underscoring the markedly enhanced cycling robustness of the EDA-modified cathode. The rate capability of E(0.2)-VSe_2 is further assessed over a wide range of current densities from 50 to 2000 mA·g^{-1} (Fig. 4(d) and Fig. S14 in the ESM). Specifically, E(0.2)-VSe_2 delivers discharge capacities of 129.6, 138.5, 132.0, 112.7, 91.3, 79.6, and 72.1 mAh·g^{-1} at current densities of 50, 100, 200, 500, 1000, 1500, and 2000 mA·g^{-1}, respectively, consistently outperforming all comparison samples. Remarkably, when the current density is restored to 50 mA·g^{-1}, the specific capacity further increases to 159.5 mAh·g^{-1}, which indicates excellent reversibility and minimal kinetic degradation. Such outstanding rate performance demonstrates the exceptional tolerance of E(0.2)-VSe_2 to high-current operation and highlights that EDA-mediated interlayer engineering enhances the structural stability of the host, thereby enabling rapid ion-transport kinetics.

The superior electrochemical stability of E(0.2)-VSe_2 is further corroborated by self-discharge measurements (Figs. 4(e) and 4(f)). After the 1st and 100th cycles, the open-circuit voltage of the E(0.2)-VSe_2 cathode decreases by 0.82 and 1.03 V, respectively, following a 72 h rest period, corresponding to low self-discharge rates of 11.4 and 14.3 mV·h^{-1}. In comparison, the pristine VSe_2 cathode exhibits higher self-discharge rates of 12.9 and 15.7 mV·h^{-1} under identical conditions. This suppressed self-discharge behavior is attributed to the enhanced structural integrity of the host lattice and the more uniform charge distribution induced by EDA intercalation [49]. Beyond short-term stability, E(0.2)-VSe_2 also shows outstanding long-term durability. At a high current density of 1000 mA·g^{-1}, the cathode sustains a capacity of 82.5 mAh·g^{-1} over 4500 continuous cycles, corresponding to a capacity retention of 72.7% relative to its maximum capacity (Fig. 4(g)). This long-term performance significantly surpasses that of most previously reported MLHB cathodes (Fig. 4(h) and Table S3 in the ESM). The charge–discharge profiles at the 4500th cycle closely resemble those observed after the activation stage, albeit with moderate polarization (Fig. S15 in the ESM), indicating highly reversible electrochemical processes. These results confirm that an optimal EDA content effectively reinforces the structural stability of the VSe_2 framework during prolonged cycling. Excessive EDA intercalation, while further enlarging the interlayer spacing, compromises the mechanical integrity of the host lattice, thereby hindering sustained ion intercalation/extraction. Conversely, insufficient EDA content results in inadequate interlayer spacing and a weak pillaring effect, failing to provide the structural stability required for long-term cycling performance.

In addition, electrochemical measurements were extended to evaluate the performance under high active mass loading conditions (Fig. S16 in the ESM). Even with a substantial increase in active material loading to 3.5 mg·cm^{-2}, the E(0.2)-VSe_2 electrode maintains a remarkable storage capability. After 400 cycles at 200 mA·g^{-1}, it retains a specific capacity of 115.9 mAh·g^{-1}, demonstrating excellent cycling stability despite the high mass loading. We also evaluated the performance of pristine VSe_2 and E(0.2)-VSe_2 cathodes in the RMB configuration (Figs. S17 and S18 in the ESM). Regrettably, both electrodes deliver negligible capacity in the RMB configuration, which is attributed to the absence of Li^+ synergy that is crucial for effective charge transfer in this system [18, 50–52]. However, when applied in aqueous copper-ion batteries (ACIB), E(0.2)-VSe_2 demonstrates outstanding electrochemical performance (Fig. S19 in the ESM). It exhibits rapid ion storage kinetics, delivering an impressive capacity of 225.4 mAh·g^{-1} at a high current density of 20 A·g^{-1}. Furthermore, the E(0.2)-VSe_2 electrode exhibits excellent cycling stability in the ACIB and maintains a capacity of 505.1 mAh·g^{-1} after 800 cycles at 5 A·g^{-1}. The fact that this capacity exceeded the theoretical value strongly suggests the involvement of a conversion reaction mechanism in the copper battery system. Owing to the reinforced interlayer modification, the E(0.2)-VSe_2 electrode maintains high specific capacities of 470 and 154.2 mAh·g^{-1} at current densities of 10 and 20 A·g^{-1} after 8000 and 17,000 cycles, respectively, with a Coulombic efficiency close to 100%.

The exceptional stability and rate performance of E(0.2)-VSe_2 are attributed to the favorable ion/electron transport environment created by the interlayer modification. Pristine VSe_2 exhibits sluggish kinetics, which results in poor practical rate performance and battery stability. To further investigate the storage kinetics of guest ions, the cyclic voltammetry (CV) curves for the 1st and 100th cycles were first analyzed at scan rates ranging from 0.2 to 1 mV·s^{-1}. As a result of the activation process in the E(0.2)-VSe_2 cathode, the peak current response in the first cycle is notably weaker than that of pristine VSe_2 (Figs. S20(a) and S21(a) in the ESM). The linear relationship observed in the Randles–Sevcik plot (Figs. S20(b) and S21(b) in the ESM) confirms the presence of diffusion-controlled guest-ion storage behavior in both electrodes. To evaluate the contributions of diffusion and pseudo-capacitance to the overall charge storage mechanism, the kinetic parameter (b) value was calculated using the equation $I(V) = av^b$, where I is the peak current,

V is the given potential, a is an adjustable constant, and v is the scan rate. The b value serves as a critical indicator for identifying the predominant charge storage mechanism, distinguishing between diffusion-controlled processes (b = 0.5) and capacitive effects (b = 1). For E(0.2)-VSe_2, the b values for the redox peaks are 0.81 and 0.91 (Fig. S21(c) in the ESM), indicating that both diffusion and capacitive behaviors contribute significantly to its electrochemical performance. These values are close to 1 and higher than those of pristine VSe_2 (Fig. S20(c) in the ESM), which exhibits b values of 0.78 and 0.82.

A consistent trend is observed after 100 cycles (Figs. S22 and S23 in the ESM). The variation observed in the CV curves shown in Fig. S23(a) in the ESM will be further explained in the following section. The capacitive contribution was further quantified based on the equation $I(V) = k_1v + k_2v^{1/2}$, where k_1 and k_2 are constants corresponding to the capacitive and diffusion-controlled contributions, respectively, as shown in Fig. 5(a). With increasing scan rate, the pseudocapacitive contribution increases accordingly. E(0.2)-VSe_2 displays a stronger pseudocapacitive contribution in both the initial cycle and the 100th cycle, and this behavior becomes more pronounced by the 100th cycle. This enhanced capacitive behavior endows E(0.2)-VSe_2 with excellent reaction kinetics and outstanding rate performance.

The desolvation of guest ions and their migration through the cathode–electrolyte interphase (CEI) are generally considered the rate-determining steps in the cathode redox process [53, 54]. The associated energy barrier can be quantified using the activation energy (E_a) in the Arrhenius equation

$$\frac{1}{R_{ct}} = Ae^{-\left(\frac{E_a}{RT}\right)} \quad (1)$$

where R_{ct} is the charge transfer resistance at the CEI, and A, R, and T represent the frequency factor, the gas constant, and the absolute temperature, respectively. As shown in Fig. 5(b), the E_a for E(0.2)-VSe_2 is calculated to be 22.38 kJ·mol^{-1}, which is significantly lower than that of pristine VSe_2 (31.9 kJ·mol^{-1}). The lower E_a suggests that the EDA interlayer modification in E(0.2)-VSe_2 promotes the formation of a favorable interfacial environment for guest ions, which accelerates their desolvation and migration through the CEI. Consequently, the electrochemical activity of E(0.2)-VSe_2 is enhanced.

The intercalation and extraction of Mg^{2+}, with its high charge

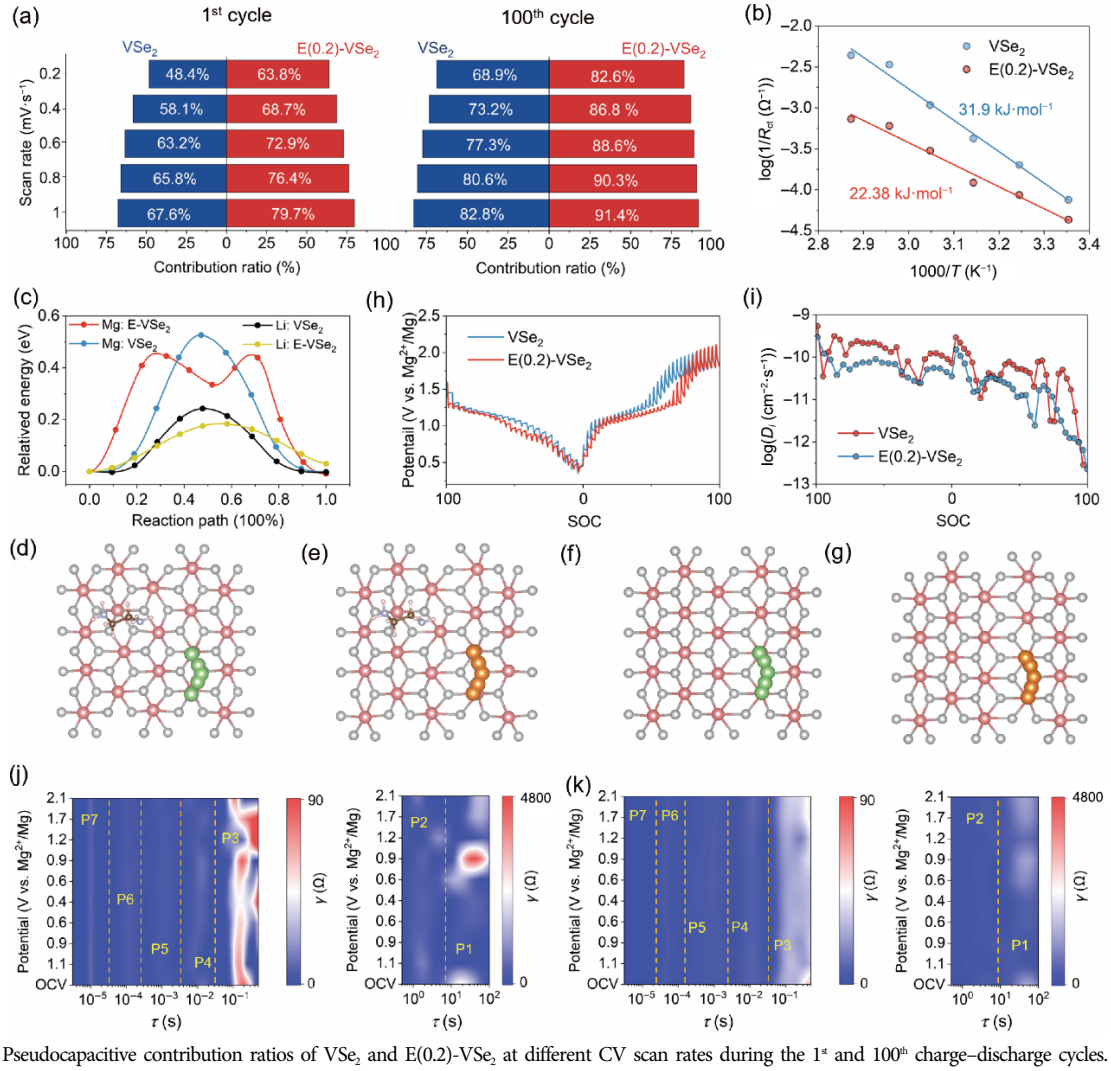

Figure 5 (a) Pseudocapacitive contribution ratios of VSe_2 and E(0.2)-VSe_2 at different CV scan rates during the 1st and 100th charge–discharge cycles. (b) Activation energy of VSe_2 and E(0.2)-VSe_2. (c) Migration energy barriers and corresponding migration paths of Mg^{2+}/Li^+ within the interlayers of ((d) and (e)) E(0.2)-VSe_2 and ((f) and (g)) VSe_2. (h) GITT curves and (i) corresponding ion diffusion coefficients of guest ions in the VSe_2 and E(0.2)-VSe_2. DRT distribution for (j) pristine VSe_2 and (k) E(0.2)-VSe_2 during the 100th cycle.

density, typically induce irreversible collapse of the host structure and high intercalation barrier, resulting in poor cycling stability and insufficient capacity. The expanded interlayer spacing and the presence of EDA weaken the Coulombic interactions between the host layers and guest ions, thereby improving the diffusion kinetics of the intercalated E(0.2)-VSe_2 cathode. To quantify these effects, the diffusion energy barriers for Li^+ and Mg^{2+} within the interlayers were compared (Fig. 5(c)), and the corresponding diffusion paths are shown in Figs. 5(d)–5(g). These calculations show that the diffusion energy barriers for Li^+ and Mg^{2+} decrease to 0.18 and 0.46 eV, respectively. Accordingly, ionic diffusion kinetics are significantly enhanced after interlayer modification. This result is directly supported by the galvanostatic intermittent titration technique (GITT) test data (Figs. 5(h)–5(i)), which confirms that the diffusion coefficient of guest ions in the E(0.2)-VSe_2 interlayer is substantially higher than that in the pristine structure. The faster and smoother diffusion process also contributes to the preservation of the stable layered structure, thereby enabling durable and reversible mixed-ion storage.

The EDA interlayer modification is also demonstrated to be effective in enhancing interfacial stability. The evolution of impedance during charging/discharging process was analyzed using *in-situ* electrochemical impedance spectroscopy (EIS). The 10^{th} and 100^{th} cycles were selected to represent early and stabilized cycling stages, respectively. Both electrodes show a decrease in overall impedance during the discharge process, and the impedance returns to higher values after charging (Figs. S24(a), S24(c), and S25 in the ESM). This trend indicates that the intercalation of guest ions facilitates charge transfer.

To gain deeper insights, distribution of relaxation times (DRT) analysis was employed to deconvolute the frequency-domain signal of EIS into time-domain responses. This approach enables precise identification of different impedance contributions in electrochemical processes, thereby improving the accuracy of kinetic interpretation on the time scale [55]. As shown in Figs. 5(j) and 5(k), the response Peaks P1 and P2 are attributed to diffusion impedance, while Peaks P3 and P4 correspond to charge-transfer impedance. Peaks P5 and P6 represent the impedance associated with guest ions crossing and migrating through the CEI film, while Peak P7 signifies the contact resistance within the system. The presence of two separated peaks within these specific processes may originate from the distinct kinetic responses of different guest ions. During the 10^{th} discharge process (Figs. S24(b) and S24(d) in the ESM), the E(0.2)-VSe_2 cathode exhibits lower diffusion resistance and charge transfer resistance before 0.9 V, demonstrating the intrinsic advantage of rapid charge-transfer in E(0.2)-VSe_2, as the influence of guest ion intercalation is minimal at this stage. In subsequent cycles, the intensities of various process peaks for the E(0.2)-VSe_2 cathode closely match those of the pristine VSe_2 cathode. This similarity is attributed to the larger amount of guest-ion intercalation accommodated by pristine VSe_2 during the initial charging/discharging cycles, which temporarily enhances its charge-transport processes.

After 100 cycles, the E(0.2)-VSe_2 cathode shows enhanced kinetics, as evidenced by the consistently weaker intensities of the response peaks across all relaxation-time domains in the DRT analysis compared with pristine VSe_2 (Figs. 5(j) and 5(k)). The weaker diffusion constraints for guest ions within the E(0.2)-VSe_2 interlayer contribute to a higher bulk diffusion rate. Furthermore, the low activation energy and the presence of Se vacancies collectively increase the reaction rate and significantly reduce the charge transfer resistance. The negligible change in CEI-related impedance suggests that the interlayer modification has a limited effect on CEI regulation. The higher internal resistance observed in the pristine VSe_2 cathode is attributed to the degradation of the interlayer structure.

The evolution of EIS spectra and corresponding DRT results in the discharged state over 200 cycles further reveals the progression of electrode storage kinetics and their stability with cycling (Figs. S26(a)–S26(d) in the ESM). Throughout the cycling period, the E(0.2)-VSe_2 cathode consistently maintains a superior kinetic advantage over the pristine VSe_2 cathode in each time domain. As cycling proceeds, the reactivity of the E(0.2)-VSe_2 electrode gradually increases, with charge transfer kinetics continuing to strengthen. This trend is reflected by the weakening of response peak intensities across various time domains, confirming a highly reversible and rapid guest-ion storage process within the electrode. In contrast, the pristine VSe_2 cathode exhibits high diffusion resistance and charge-transfer impedance during cycling. These features indicate increased interfacial reaction resistance caused by interlayer structural instability and interfacial passivation, which severely hinders ion transport. Therefore, the unique interlayer environment of E(0.2)-VSe_2 enables rapid and stable kinetics, ensuring durable guest ion storage.

Revealing the guest-ion storage mechanism of the E(0.2)-VSe_2 electrode can provide crucial insights into the origin of its exceptional stability and rapid reaction kinetics. To illustrate the effect of EDA intercalation on the redox behavior of VSe_2, CV tests were performed on both electrodes within the voltage range of 0.4–2.1 V (Fig. S27 in the ESM). During the initial three cycles, the E(0.2)-VSe_2 electrode exhibits weaker redox peaks and a slightly smaller integrated area compared with that of pristine VSe_2, which is consistent with the lower capacity observed during this period. However, this trend reverses during cycles 100–103. The CV area of pristine VSe_2 decreases, with its redox peaks becoming less distinct, whereas the redox peaks of E(0.2)-VSe_2 become more intense, and exhibit higher response currents and larger peak areas. These results indicate improved active material utilization with cycling, suggesting superior reaction kinetics and increased guest-ion storage capacity.

Meanwhile, new reduction peaks emerge near 0.75 and 0.83 V, corresponding to the reduction of V^{3+} to V^{2+} during the discharge process enabled by EDA intercalation. The emergence of these two peaks suggests large-scale intercalation of guest ions, causing the reduction process to proceed in stages, and favoring the minimization of the energy required to open the interlayer van der Waals gaps [56, 57]. This additional redox contribution also explains why the measured capacity exceeds the theoretical value based on single-electron transfer (128 $mAh \cdot g^{-1}$). During the oxidation process, the transformation of V^{2+} to V^{4+} occurs in one step within the broad oxidation peak [58]. Furthermore, *ex-situ* XPS analysis of the V 2p region from the 1^{st} and 100^{th} cycles (Fig. S28 in the ESM) confirms V-centered redox reactions throughout the electrochemical process, specifically between V^{4+} and V^{2+}, which provides additional support for the above interpretation. In addition, the absence of a V^{2+} signal during the first discharge, in contrast to its appearance after 100 cycles, can be attributed to the insufficient reaction at the initial stage. Because only a limited amount of guest ions is stored in the host during the early stage, the reduction of VSe_2 remains incomplete and is mainly confined to the

V^{4+}/V^{3+} redox couple. The relatively low capacity in the first discharge further supports this interpretation, as the smaller capacity corresponds to fewer transferred electrons and is therefore insufficient to drive the further reduction of V^{3+} to V^{2+}. After electrochemical activation during cycling, however, the discharge reaction proceeds to a greater depth, and the specific capacity increases markedly, corresponding to more substantial electron injection and deeper reduction of vanadium. As a result, the formation of V^{2+} becomes detectable during the 100th discharge. In addition, during discharge, the two characteristic V 2p peaks shift progressively to lower binding energies, indicating charge redistribution around V atoms resulting from guest ion intercalation.

The *ex-situ* high-resolution XPS spectra of the cathode further reveal the mixed-ion storage behavior in the E(0.2)-VSe_2 host. In the pristine state, Se 3d spin-orbital splitting peaks appear at 53.6 and 54.5 eV (Fig. 6(a)), and no detectable Li 1s signal is observed. Reversible Li^+ intercalation is confirmed by the appearance and disappearance of the Li 1s peak after the first discharge/charge process. This behavior remains highly reversible even after the

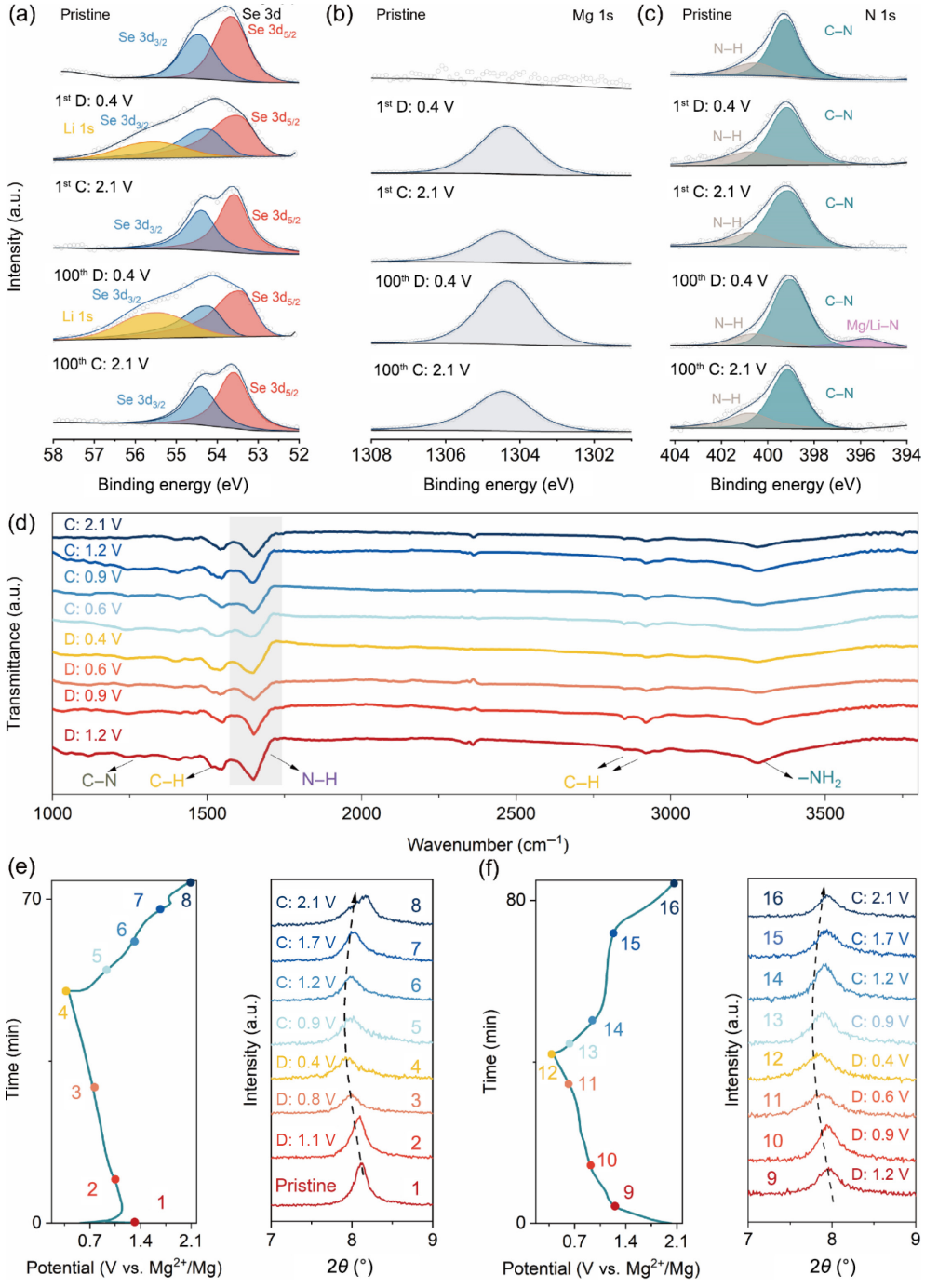

Figure 6 *Ex-situ* XPS spectra of E(0.2)-VSe_2 at different charging (C)/discharging (D) states in pristine, 1st, and 100th cycle, including (a) Se 3d (Li 1s), (b) Mg 1s, and (c) N 1s. (d) *Ex-situ* FTIR spectra of E(0.2)-VSe_2 cathode at different charging and discharging voltages during the 100th cycle. *Ex-situ* XRD patterns of E(0.2)-VSe_2 cathode at (e) the first cycle and (f) 100th cycle.

100th cycle. The reversible shifts of the Se $3d_{3/2}$ and Se $3d_{5/2}$ peaks further confirm reversible intercalation/deintercalation in the cathode and interaction with Se. Additionally, the significant increase in the intensity of the Li 1s peak confirms the enhanced Li^+ storage. Benefiting from Li^+ intercalation, the intercalation behavior of Mg^{2+} is also improved. Reversible intercalation/extraction of Mg^{2+} is observed in both the 1st and 100th cycles, and the intensity of the Mg 1s signal increases/decreases upon discharge/charge completion (Fig. 6(b)). Furthermore, the detected Cl 2p peak shows negligible fluctuations throughout the entire charge–discharge process, and the persistent signals are attributed to residual electrolyte components on the surface (Fig. S29 in the ESM). Therefore, the interlayer modification does not alter the type of intercalating ions in VSe_2 (Fig. S30 in the ESM). Inductively coupled plasma mass spectrometry (ICP-MS) results (Table S4 in the ESM) quantitatively support the XPS findings. Meanwhile, the capacity contributions from Mg^{2+} and Li^+ at different cycling stages can be quantified. During the initial discharge, Li^+ and Mg^{2+} each contribute 0.22 of the transferred electrons (50% of the capacity each). By the 100th cycle, the contributions of Li^+ and Mg^{2+} increase to 0.7 and 0.53 electrons (contributing 56.9% and 43.1% of the capacity, respectively), which is consistent with the experimentally measured capacity. These results further exclude $MgCl^+$ intercalation.

It is noteworthy that E(0.2)-VSe_2 exhibits an organic–inorganic dual storage mechanism, as evidenced by the N 1s XPS spectra (Fig. 6(c)). Upon discharge to 0.4 V in the 100th cycle, the formation of an N–Mg/Li peak at 395.9 eV is clearly observed, indicating an interaction between the guest ions and EDA. This peak disappears by the end of the charge process, demonstrating that the guest-ion storage behavior of EDA is reversible. No detectable N–Mg/Li XPS signal is observed in the first cycle, which is attributed to the insufficient electrochemical reactions during the initial stage.

Ex-situ FTIR results further support this finding. During the first cycle, all characteristic vibrational peaks of the EDA molecules remain essentially unchanged in the FTIR spectra (Fig. S31 in the ESM), due to the limited extent of reaction. However, after 100 cycles, the N–H bending vibration peak at 1650.8 cm^{-1} gradually weakens upon discharge. This originates from the formation of chelate rings upon coordination of Mg^{2+}/Li^+ with EDA, which suppresses the N–H bending vibration [40, 59]. These spectral features fully recover to their original intensities during the subsequent charge process (Fig. 6(d)). Such a reversible organic–inorganic composite storage mechanism plays a critical role in enabling the outstanding electrochemical performance of E(0.2)-VSe_2.

To elucidate the structural response of the material during electrochemical cycling, *ex-situ* XRD patterns were employed to track the evolution of the crystal structure at different voltage states. As shown in Fig. 6(e), during the first discharge process, the (001) peak shifts gradually to a lower angle (7.92°, corresponding to a *d*-spacing of 1.12 nm), indicating interlayer expansion induced by Mg^{2+}/Li^+ intercalation. Upon subsequent charging, the (001) peak progressively returns toward its original position (8.78°, corresponding to a *d*-spacing of 1.08 nm), demonstrating highly reversible deintercalation of Mg^{2+}/Li^+. The structural evolution during the 100th discharge closely mirrors that of the first cycle (Fig. 6(f)), confirming the excellent stability of the layered framework. However, owing to cumulative cycling effects, a small fraction of guest ions remains trapped within the interlayers. Consequently, compared with the first charge–discharge process, the overall (001) peak position shifted slightly toward lower angles (discharged to 0.4 V: 7.85°, 1.13 nm; charged to 2.1 V: 7.97°, 1.11 nm). Analysis of the remaining diffraction peaks (Fig. S32 in the ESM) reveals no evidence of new crystalline phases associated with selenide formation, such as Li_2Se or MgSe, throughout the electrochemical process. This observation indicates that Mg^{2+}/Li^+ storage in the E(0.2)-VSe_2 host proceeds via a topotactic intercalation mechanism, consistent with the behavior observed in pristine VSe_2 cathodes (Fig. S33 in the ESM).

3 Conclusions

In this work, we propose a molecular interlayer engineering strategy based on EDA intercalation to optimize the guest-ion storage environment of VSe_2 cathodes. The EDA molecules act as robust molecular pillars that expand the interlayer spacing, thereby constructing stable and spacious diffusion channels for Mg^{2+}/Li^+ transport. The modulation of the electronic structure, generation of abundant Se vacancies, and attenuation of interlayer Coulombic interactions collectively accelerate guest-ion transport and reaction kinetics. Furthermore, the electron-rich $–NH_2$ groups enable reversible bidentate chelation with intercalated Mg^{2+}/Li^+, providing additional active storage sites. This enables the electrode to achieve an organic–inorganic synergistic storage mechanism based on Mg^{2+}/Li^+ co-intercalation. *Ex-situ* characterizations confirm the high reversibility of this topological evolution and the excellent preservation of structural integrity upon prolonged cycling. As a result of these synergistic effects, the E(0.2)-VSe_2 cathode exhibits outstanding rate capability and markedly enhanced cycling stability. More broadly, this work establishes a general and powerful design paradigm for layered electrode materials toward efficient and durable multivalent-ion storage.

Electronic Supplementary Material: Supplementary material (experimental details, DFT calculations, XPS, TGA, EPR, DRT, and other supplementary characterizations, as well as additional battery performance tests) is available in the online version of this article at https://doi.org/10.26599/NR.2026.94908829.

Data availability

All data needed to support the conclusions in the paper are presented in the manuscript and the Electronic Supplementary Material. Additional data related to this paper may be requested from the corresponding author upon request.

Acknowledgements

This work was supported by the National Natural Science Foundation of China (No. T2527901) and Hubei Provincial Science and Technology Infrastructure Platform Special Program (No. 2025CSA058). Z. D. L. acknowledges funding support from the Start-up Fund from Wuhan University and the Hubei Province "Chutian Talent Plan" Science and Technology Innovation Team Project. The authors thank Dr. Lili Dai, Dr. Yanli Guo, Dr. Xuesong Feng, Dr. Mingyuan Du, and Dr. Jie Hu from the Core Facility of Wuhan University for their assistance with XPS, SEM, ICP, FTIR, and XRD measurements and data analysis. The authors also thank the School of Integrated Circuits of Wuhan University for XRD analysis.

Declaration of competing interest

All the contributing authors report no conflict of interests in this work.

Author contribution statement

J.-L. L.: Conceptualization, data curation, formal analysis, investigation, methodology, software, writing – original draft, writing – review & editing. L.-R. W.: Formal analysis, investigation, software, validation, visualization. Y.-Q. J.: Formal analysis, investigation, methodology, validation, visualization. C.-Y. C.: Formal analysis, investigation, software, visualization. H.-N. S.: Investigation, methodology, resources. Y.-J. X.: Methodology, resources, validation. Z.-D. L.: Conceptualization, data curation, formal analysis, funding acquisition, methodology, project administration, resources, supervision, writing – review & editing. S. L.: Data curation, funding acquisition, project administration, resources, supervision. All the authors have approved the final manuscript.

Use of AI statement

None.

References

[1] Li, Y. J.; Kumar, S.; Yang, G. L.; Lu, J.; Yao, Y.; Kang, K.; Seh, Z. W. The contrast between monovalent and multivalent metal battery anodes. *Science* **2025**, *389*, eadl5482.

[2] Zhang, J. R.; Liu, M. L.; Qi, J. C.; Lei, N.; Guo, S. R.; Li, J. F.; Xiao, X. Z.; Ouyang, L. Z. Advanced Mg-based materials for energy storage: Fundamental, progresses, challenges and perspectives. *Prog. Mater. Sci.* **2025**, *148*, 101381.

[3] Li, M.; Lu, J.; Ji, X. L.; Li, Y. G.; Shao, Y. Y.; Chen, Z. W.; Zhong, C.; Amine, K. Design strategies for nonaqueous multivalent-ion and monovalent-ion battery anodes. *Nat. Rev. Mater.* **2020**, *5*, 276–294.

[4] Sun, Q.; Luo, S. H.; Huang, R.; Yan, S. X.; Lin, X. P. Recent progress of magnesium electrolytes for rechargeable magnesium batteries. *Coord. Chem. Rev.* **2024**, *515*, 215956.

[5] Gohar, O.; Ishfaq, H. A.; Iqbal, M. A.; Khan, M. Z.; Basharat, S.; Kanwal, N.; Riaz, A.; Saleem, M.; Koh, J. H.; Hussain, I. et al. Recent advancements in high-performance and durable electrodes materials for magnesium-ion batteries. *Coord. Chem. Rev.* **2025**, *538*, 216702.

[6] Luo, L. X.; Xia, L. Y.; Tan, S. S.; Sun, R. M.; He, Z.; Huang, X. T.; Gao, Z. P.; Huang, J.; Zhang, Y. F.; Yang, X. F. et al. Co-intercalation of solvated Mg^{2+} in amine-chain-expanded $VOPO_4$ cathodes with fast kinetics under high-voltage condition. *Energy Storage Mater.* **2025**, *77*, 104209.

[7] Li, G. Y.; Cao, L.; Lei, M.; Chen, K. Y.; Li, C. L. Customizing vertical electrodeposition orientation and interfacial solvation to endow magnesium metal anodes with ultrahigh areal capacity. *Energy Environ. Sci.* **2025**, *18*, 7254–7266.

[8] Wang, Y. Q.; Cheng, F. L.; Ji, J. W.; Cai, C. Y.; Fu, Y. Reshaping Li–Mg hybrid batteries: Epitaxial electrodeposition and spatial confinement on MgMOF substrates via the lattice-matching strategy. *Carbon Energy* **2024**, *6*, e520.

[9] Roy, A.; Sotoudeh, M.; Dinda, S.; Tang, Y. S.; Kübel, C.; Groß, A.; Zhao-Karger, Z.; Fichtner, M.; Li, Z. Y. Improving rechargeable magnesium batteries through dual cation co-intercalation strategy. *Nat. Commun.* **2024**, *15*, 492.

[10] Wang, T.; Li, M. S.; Qi, L.; Jie, P. F.; Yang, W. L.; Li, Y. L. Multilevel heterostructure of MoS_2/GDYO for lithium-ion batteries. *Adv. Funct. Mater.* **2023**, *33*, 2308470.

[11] Xu, J.; Zhang, J. J.; Zhang, W. J.; Lee, C. S. Interlayer nanoarchitectonics of two-dimensional transition-metal dichalcogenides nanosheets for energy storage and conversion applications. *Adv. Energy Mater.* **2017**, *7*, 1700571.

[12] Li, Y. Q.; Xiao, S. S.; Qiu, T. Y.; Lang, X. Y.; Tan, H. Q.; Wang, Y. H.; Li, Y. G. Recent advances on energy storage microdevices: From materials to configurations. *Energy Storage Mater.* **2022**, *45*, 741–767.

[13] Wu, J. J.; Peng, J.; Sun, H. F.; Guo, Y. Q.; Liu, H. F.; Wu, C. Z.; Xie, Y. Host–guest intercalation chemistry for the synthesis and modification of two-dimensional transition metal dichalcogenides. *Adv. Mater.* **2022**, *34*, 2200425.

[14] Zhang, Z. P.; Niu, J. J.; Yang, P. F.; Gong, Y.; Ji, Q. Q.; Shi, J. P.; Fang, Q. Y.; Jiang, S. L.; Li, H.; Zhou, X. B. et al. van der Waals epitaxial growth of 2D metallic vanadium diselenide single crystals and their extra-high electrical conductivity. *Adv. Mater.* **2017**, *29*, 1702359.

[15] Salavati, M.; Rabczuk, T. Application of highly stretchable and conductive two-dimensional 1T VS_2 and VSe_2 as anode materials for Li-, Na- and Ca-ion storage. *Comput. Mater. Sci.* **2019**, *160*, 360–367.

[16] Yang, C.; Feng, J. R.; Lv, F.; Zhou, J. H.; Lin, C. F.; Wang, K.; Zhang, Y. L.; Yang, Y.; Wang, W.; Li, J. B. et al. Metallic graphene-like VSe_2 ultrathin nanosheets: Superior potassium-ion storage and their working mechanism. *Adv. Mater.* **2018**, *30*, 1800036.

[17] Sha, D. W.; You, Y. R.; Hu, R. X.; Cao, X.; Wei, Y. C.; Zhang, H.; Pan, L.; Sun, Z. M. Comprehensively understanding the role of anion vacancies on K-ion storage: A case study of Se-vacancy-engineered VSe_2. *Adv. Mater.* **2023**, *35*, 2211311.

[18] Li, J. L.; Wang, L. R.; Jiang, Y. Q.; Ren, Y. Q.; Xu, B. Q.; Cai, Y.; Lu, S. C.; Chen, C. Y.; Song, H. N.; He, J. L. et al. Molecular-level interface engineering of VSe_2 self-supporting architectures enables durable Mg^{2+}/Li^+ co-intercalation. *J. Energy Chem.* **2026**, *113*, 266–277.

[19] Wang, Y. R.; Liu, Z. T.; Wang, C. X.; Yi, X.; Chen, R. P.; Ma, L. B.; Hu, Y.; Zhu, G. Y.; Chen, T.; Tie, Z. X. et al. Highly branched VS_4 nanodendrites with 1D atomic-chain structure as a promising cathode material for long-cycling magnesium batteries. *Adv. Mater.* **2018**, *30*, 1802563.

[20] Chen, D.; Shen, J. W.; Li, X.; Cao, S. A.; Li, T.; Luo, W.; Xu, F. $Ni_{0.85}Se$ hexagonal nanosheets as an advanced conversion cathode for Mg secondary batteries. *J. Energy Chem.* **2020**, *48*, 226–232.

[21] Zhu, G. L.; Xia, G. L.; Pan, H. G.; Yu, X. B. Size-controllable nickel sulfide nanoparticles embedded in carbon nanofibers as high-rate conversion cathodes for hybrid Mg-based battery. *Adv. Sci.* **2022**, *9*, 2106107.

[22] Li, R.; Xia, L. Y.; Yue, J. L.; Wu, J. H.; Teng, X. X.; Chen, J.; Huang, G. S.; Wang, J. F.; Pan, F. S. Nanosized anatase TiO_2 with exposed (001) facet for high-capacity Mg^{2+} ion storage in magnesium ion batteries. *Nano-Micro Lett.* **2026**, *18*, 17.

[23] Xu, A.; Liu, Y.; Wang, J. H.; Wang, Y. J.; Jiang, F. Y.; Zhou, Y. L. Highly defective and conductive Cu-doped 1T/2H-MoS_2 nanosheets as high-capacity cathode materials for enhanced magnesium-ion storage. *Inorg. Chem. Front.* **2024**, *11*, 7831–7842.

[24] Fan, X.; Tebyetekerwa, M.; Wu, Y. L.; Gaddam, R. R.; Zhao, X. S. Origin of excellent charge storage properties of defective tin disulphide in magnesium/lithium-ion hybrid batteries. *Nano-Micro Lett.* **2022**, *14*, 177.

[25] Chen, F. Y.; Huang, K. F.; Li, H. Y.; Zhong, Q.; Yue, J. L.; Diao, J.; Wang, Z. T.; Huang, G. S.; Jiang, B.; Pan, F. S. Interlayer cationic defect engineering in lamellar vanadate cathodes enables ultralong-lifespan magnesium-ion batteries. *ACS Energy Lett.* **2025**, *10*, 2052–2060.

[26] Wang, W. X.; Jiang, Y. L.; Yang, Y.; Xiong, F. Y.; Zhu, S. H.; Wang, J. J.; Du, L. L.; Chen, J. H.; Cui, L. M.; Xie, J. et al. Basal planes unlocking and interlayer engineering endows proton doped-$MoO_{2.8}F_{0.2}$ with fast and stable magnesium storage. *ACS Nano* **2022**, *16*, 17097–17106.

[27] Mao, M. L.; Ji, X.; Hou, S.; Gao, T.; Wang, F.; Chen, L.; Fan, X. L.; Chen, J.; Ma, J. M.; Wang, C. S. Tuning anionic chemistry to improve kinetics of Mg intercalation. *Chem. Mater.* **2019**, *31*, 3183–3191.

[28] Xu, Y. N.; Xu, C.; An, Q. Y.; Wei, Q. L.; Sheng, J. Z.; Xiong, F. Y.;

Pei, C. Y.; Mai, L. Q. Robust $LiTi_2(PO_4)_3$ microflowers as high-rate and long-life cathodes for Mg-based hybrid-ion batteries. *J. Mater. Chem. A* **2017**, *5*, 13950–13956.
[29] Li, J. W.; McColl, K.; Lu, X. K.; Sathasivam, S.; Dong, H. B.; Kang, L. Q.; Li, Z. N.; Zhao, S. Y.; Kafizas, A. G.; Wang, R. et al. Multi-scale investigations of δ-$Ni_{0.25}V_2O_5{\cdot}nH_2O$ cathode materials in aqueous zinc-ion batteries. *Adv. Energy Mater.* **2020**, *10*, 2000058.
[30] Pang, Q.; He, W.; Yu, X. Y.; Yang, S. Y.; Zhao, H. N.; Fu, Y.; Xing, M. M.; Tian, Y.; Luo, X. X.; Wei, Y. J. Aluminium pre-intercalated orthorhombic V_2O_5 as high-performance cathode material for aqueous zinc-ion batteries. *Appl. Surf. Sci.* **2021**, *538*, 148043.
[31] Sun, Y. N.; Åvall, G.; Wu, S. H.; A. Ferrero, G. ; Freytag, A.; Groszewicz, P. B.; Wang, H.; Mazzio, K. A.; Bianchini, M.; Baran, V. et al. Solvent co-intercalation in layered cathode active materials for sodium-ion batteries. *Nat. Mater.* **2025**, *24*, 1441–1449.
[32] Deng, R. R.; Wang, Z. T.; Tan, S. S.; Huang, X. T.; Gao, Z. P.; Fang, Y. H.; Chen, C. F.; Wang, R. H.; Xu, C. H.; Huang, G. S. et al. Optimization of the electrode reaction kinetics of V_2O_5 via polyacrylonitrile intercalation for high-performance magnesium batteries. *Chem. Eng. J.* **2024**, *489*, 151095.
[33] Li, G. Y.; Yao, Z. G.; Li, C. L. *In-situ* multi-scale structural engineering of cathode and electrolyte for high-rate and long-life Mg metal batteries. *J. Energy Chem.* **2025**, *105*, 44–53.
[34] Zhang, X.; Liu, J. C.; Liu, Y. N.; Zhu, Y. F.; Zhang, J. G.; Wang, J.; Shi, R. Dual strategy of morphology optimization and interlayer expansion in VS_2 cathode toward high-performance Mg–Li hybrid ion batteries. *ACS Appl. Mater. Interfaces* **2024**, *16*, 36401–36412.
[35] Jing, P. C.; Lu, H. M.; Yang, W. W.; Cao, Y. Interlayer-expanded and binder-free VS_2 nanosheets assemblies for enhanced Mg^{2+} and Li^+/Mg^{2+} hybrid ion storage. *Electrochim. Acta* **2020**, *330*, 135263.
[36] Tang, H.; Xiong, F. Y.; Jiang, Y. L.; Pei, C. Y.; Tan, S. S.; Yang, W.; Li, M. S.; An, Q. Y.; Mai, L. Alkali ions pre-intercalated layered vanadium oxide nanowires for stable magnesium ions storage. *Nano Energy* **2019**, *58*, 347–354.
[37] Tang, H. W.; Wan, K. X.; Zhang, K.; Wang, A.; Wang, M. K.; Xie, J.; Su, P. C.; Dong, H. L.; Sun, J. Y.; Li, Y. H. Realizing dual-mode zinc-ion storage of generic vanadium-based cathodes via organic molecule intercalation. *ACS Nano* **2024**, *18*, 30896–30909.
[38] Cui, F. Y.; Li, J. Z.; Lai, C.; Li, C. Z.; Sun, C. H.; Du, K.; Wang, J. S.; Li, H. Y.; Huang, A. M.; Peng, S. J. et al. Superlattice cathodes endow cation and anion co-intercalation for high-energy-density aluminium batteries. *Nat. Commun.* **2024**, *15*, 8108.
[39] Ma, X. M.; Cao, X. X.; Yao, M. L.; Shan, L. T.; Shi, X. D.; Fang, G. Z.; Pan, A. Q.; Lu, B. A.; Zhou, J.; Liang, S. Q. Organic-inorganic hybrid cathode with dual energy-storage mechanism for ultrahigh-rate and ultralong-life aqueous zinc-ion batteries. *Adv. Mater.* **2022**, *34*, 2105452.
[40] Yang, C.; Chen, S. J.; Wang, K. P.; Zong, L. B.; Chen, D. H.; Wang, X. N.; Zhang, Q.; Wang, L. Polar organic molecules assisting Mo-based cathode materials for enhanced zinc-ion transfer kinetics. *Chem. Eng. J.* **2024**, *496*, 153731.
[41] Lin, Z. Y.; Zhang, W.; Peng, J.; Li, Q. H.; Liang, Z. X.; Wang, G. Y.; Wang, J. L.; Wang, G.; Huang, Z. J.; Huang, S. M. Synergistic regulation of polyselenide dissolution and Na-ion diffusion of Se-vacancy-rich bismuth selenide toward ultrafast and durable sodium-ion batteries. *Adv. Energy Mater.* **2024**, *14*, 2402110.
[42] Fu, X. X.; Yang, M.; Zhai, M. H.; Zhang, C.; Niu, H. J.; Li, Y. Q. Precision anode vacancy engineering for long-lasting and fast-charging Na-Ion batteries. *Energy Storage Mater.* **2024**, *70*, 103450.
[43] Zhao, L.; Li, Y.; Yu, M. M.; Peng, Y. Y.; Ran, F. Electrolyte-wettability issues and challenges of electrode materials in electrochemical energy storage, energy conversion, and beyond. *Adv. Sci.* **2023**, *10*, 2300283.
[44] Chen, F.; Chen, T. X.; Wu, Z. X.; Zhou, Z. H.; Lu, K. J.; Su, J. Y.; Wang, Y. H.; Hua, J. F.; Lai, X.; Han, X. B. et al. Unraveling mechanisms of electrolyte wetting process in three-dimensional electrode structures: Insights from realistic architectures. *Green Energy Intell. Transp.* **2025**, *4*, 100248.
[45] Augustyn, V.; Simon, P.; Dunn, B. Pseudocapacitive oxide materials for high-rate electrochemical energy storage. *Energy Environ. Sci.* **2014**, *7*, 1597–1614.
[46] Lyu, L.; Hu, J.; Cheng, K.; Lin, D. M.; Li, K. K.; Lu, Z. G.; Yao, H. M.; Zhou, L. M. Insights into self-induced electrochemical activation of carbon cathode. *Carbon* **2022**, *188*, 177–186.
[47] Kumar, B. V. R.; Sathyanarayana, S. The delayed action of magnesium anodes in primary batteries Part I. *Experimental studies. J. Power Sources* **1983**, *10*, 219–241.
[48] Zhang, Z. Y.; Sun, Z. H.; Sun, S. B.; Liu, J. Y.; Jiang, J. Q.; Shang, W.; Wen, Y. Q. MXene modified anode of magnesium battery to improve the problems of voltage lag and irreversibility. *J. Alloys Compd.* **2023**, *960*, 170609.
[49] Zhou, Q.; Zheng, X. L.; Lin, Y. X.; Wei, L.; Zhao, X. S.; Li, X. X. $NiCo_2O_4$@C nanowire bundles as free-standing electrode for high-performance supercapacitor with suppressed self-discharge and robust cycling stability. *J. Power Sources* **2025**, *656*, 238096.
[50] Si, W. H.; Tian, M.; Wang, Z. T.; Ma, H. P.; Du, Y. B.; Wang, W. L.; Zhang, W. M.; Yang, H. Y.; Chen, S. Dual-ion co-insertion engineering for kinetics enhancement and stress regulation in Cu_3VS_4 toward durable magnesium/lithium hybrid batteries. *Adv. Funct. Mater.* **2025**, *35*, 2411881.
[51] Gao, T.; Han, F. D.; Zhu, Y. J.; Suo, L. M.; Luo, C.; Xu, K.; Wang, C. S. Hybrid Mg^{2+}/Li^+ battery with long cycle life and high rate capability. *Adv. Energy Mater.* **2015**, *5*, 1401507.
[52] Li, H. Y.; Okamoto, N. L.; Hatakeyama, T.; Kumagai, Y.; Oba, F.; Ichitsubo, T. Fast diffusion of multivalent ions facilitated by concerted interactions in dual-ion battery systems. *Adv. Energy Mater.* **2018**, *8*, 1801475.
[53] Bai, L. S.; Xu, Y.; Liu, Y.; Zhang, D. N.; Zhang, S. B.; Yang, W. J.; Chang, Z.; Zhou, H. S. Metal–organic framework glass stabilizes high-voltage cathodes for efficient lithium-metal batteries. *Nat. Commun.* **2025**, *16*, 3484.
[54] Lu, X. J.; Chen, L.; Li, W. X.; Zhang, X. L.; Chi, W. L.; Peng, M.; Wang, C. X.; Liu, Y.; Zhang, X. W. Accelerating desolvation and constructing dual-storage channels for Zn^{2+} by ligand field engineering of polar organic molecules for high-performance zinc-ion batteries. *Adv. Funct. Mater.* **2026**, *36*, e13457.
[55] Qu, Z. L.; Luo, W. D.; Gao, C. T.; Liu, Y. F.; Shi, Z. D.; Rao, A. M.; Li, F. F.; Lu, B. A. Cryo-synthesized Prussian blue analogues as advanced cathode materials for potassium-ion batteries. *Natl. Sci. Open* **2025**, *4*, 20250022
[56] Li, Y. F.; Liang, Y. L.; Robles Hernandez, F. C.; Deog Yoo, H.; An, Q. Y.; Yao, Y. Enhancing sodium-ion battery performance with interlayer-expanded MoS_2-PEO nanocomposites. *Nano Energy* **2015**, *15*, 453–461.
[57] Newman, G. H.; Klemann, L. P. Ambient temperature cycling of an Na–TiS_2 cell. *J. Electrochem. Soc.* **1980**, *127*, 2097–2099.
[58] Fu, Q.; Azmi, R.; Sarapulova, A.; Mikhailova, D.; Dsoke, S.; Missiul, A.; Trouillet, V.; Knapp, M.; Bramnik, N.; Ehrenberg, H. Electrochemical and structural investigations of different polymorphs of TiO_2 in magnesium and hybrid lithium/magnesium batteries. *Electrochim. Acta* **2018**, *277*, 20–29.
[59] Tong, Y. X.; Zang, Y.; Su, S. D.; Zhang, Y. G.; Fang, J. Z.; Yang, Y. Q.; Li, X. M.; Wu, X.; Chen, F. M.; Hou, J. H. et al. Methylene blue intercalated vanadium oxide with synergistic energy storage mechanism for highly efficient aqueous zinc ion batteries. *J. Energy Chem.* **2023**, *77*, 269–279.